Article

Iron Electrodes Based on Sulfur-Modified Iron Oxides with Enhanced Stability for Iron−Air Batteries

Nicolás Villanueva, Cinthia Alegre,* Javier Rubin, Horacio A. Figueredo-Rodríguez,
Rachel D. McKerracher, Carlos Ponce de León, and María Jesús Lázaro*
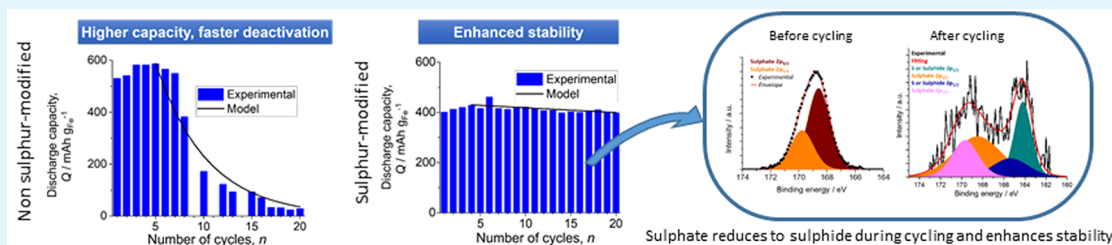
Cite This: https://doi.org/10.1021/acsaem.2c02123

Read Online

| ACCESS | | Metrics & More | | Article Recommendations | | Supporting Information |

Sulphate reduces to sulphide during cycling and enhances stability

ABSTRACT: Iron−air systems are a very promising technology with the potential to become one of the cheapest and safest energy storage solutions of the future. However, iron anodes still face some challenges like passivation, resulting in loss of capacity, due to the formation of nonconductive species during cycling as well as the hydrogen evolution reaction, a parasitic reaction interfering with the charging of the electrode. In the present work these two issues are addressed: Sulfur-modified mesoporous iron oxides are obtained and used as hot-pressed negative electrodes for alkaline iron−air batteries. Iron electrodes present average capacity values between 400 and 500 mA h g$_{Fe}^{-1}$ for ~100 h of operation, the S-modified iron oxides being the most stable ones. An exponential deactivation model fitting the discharge capacity of the different electrodes compared to the number of cycles was proposed. According to the model, the best of the electrodes loses less than 0.5% of its capacity per cycle. Furthermore, doubling the charge and discharge rates allows increasing both the discharge capacity and the Coulombic efficiency, though at the expense of stability. This manuscript proves that the proper distribution of sulfur on the surface of the iron oxide is fundamental to suppress the HER and passivation, enhancing the stability of the electrode. These properties were further corroborated in long test-runs which comprised more than 400 h of charging and discharging.

KEYWORDS: electrodes, hydrogen evolution, iron−air batteries, passivation, stability, sulfur-modified

1. BACKGROUND

In order to limit the rise of the global temperature below 1.5 °C, the Intergovernmental Panel on Climate Change (IPCC) estimates that greenhouse gas (GHG) emissions must be cut down to 25−30 Gton of CO$_2$e per year by 2030.[1] As the transport sector accounts for 29% of the total world energy consumption[2] and 72% of this sector's emissions are related to road transport,[3] the transition from oil-based mobility to electromobility will have a high importance and impact in the following years. Lithium-ion batteries are the most used power storage devices for electric vehicles, but there are still concerns related to their specific energy (commercial Li-ion batteries reach up to 248 Wh kg^{-1}), cost (>$150 USD (kW h)$^{-1}$), and safety issues such as thermal runaway,[4] causing fires and explosions.[5,6] Besides, given that lithium ion batteries need some scarce elements and the global supply chains are put under a lot of pressure, batteries made with iron are becoming more attractive.

Metal−air batteries (MABs) are an alternative promising system due to their high theoretical energy densities (from 1000 to 11 000 W h kg^{-1}). MABs consist of a negative electrode, a metal that oxidizes during discharge, an electrolyte, and a positive electrode, in which ambient oxygen is reduced. Since air/oxygen is not stored within the cell, MABs present a high theoretical gravimetric energy density and a light weight.[7] Several metals can be used as anodes, such as lithium, sodium, magnesium, potassium, aluminum, zinc, and iron. This will determine the type of electrolyte to be used: nonaqueous for Li, Na, Mg, and Al and aqueous for Zn and Fe. Among all MABs, iron−air batteries (IABs) have several advantages. The Fe−air battery is a space-saving technology due to the high theoretical volumetric energy density of iron of 9700 kW h m^{-3} (versus 270−670 kW h m^{-3} of Li-ion batteries) and iron

A

reacting directly with an aqueous electrolyte, not intercalating in a material like lithium cations. Although IABs have the lowest open circuit voltage and theoretical gravimetric specific energy of all the aforementioned systems of 1.28 V and 1080 W h kg_{Fe}^{-1}, respectively,[7] IABs have the potential to become one of the cheapest and safest energy storage solutions of the future. Iron is one of the most abundant elements in the Earth's crust (4th position),[8] is economic, is safe to handle, and is easy to refine. Besides, IABs can be electrically recharged (unlike Al−air), do not form dendrites during operation (as Zn−air), and operate with an aqueous electrolyte, usually KOH, which is cheaper than organic electrolytes and more environmentally friendly.[9,10] However, IABs still face some challenges that need to be tackled before IABs are technically and commercially viable. Challenges on the air electrode are widely known and common to other metal−air systems. On the other hand, the negative electrode of IAB presents the following problems: (a) the parasitic hydrogen evolution reaction (HER) during the charge, which reduces the Coulombic efficiency of the system, (b) the electrode passivation due to the formation of electrically nonconductive compounds (such as iron(II) hydroxide and goethite) during discharge, and (c) the molar volume change of iron discharge products related to metallic iron.

Most approaches aimed at inhibiting or reducing the rate of the HER are based on certain additives in the electrolyte like alkanethiols[11,12] or sulfide salts such as K_2S or Na_2S[13] that have been proved to effectively suppress HER. Other approaches including sulfides (FeS, Bi_2S_3, Na_2S, or K_2S)[14−18] in the iron electrode composition have shown good performances at relatively low additive concentrations (<10% wt), and it has also been established that sulfide species can also prevent passivation. However, these approaches incorporate the sulfide additives either by ball-milling (in which additives and active electrode species are merely physically mixed) or in the electrolyte (adding complexity to the design of the cell and contaminating the air electrode, as recently established[12]). In addition certain additives like those based on bismuth are not desirable since bismuth is a critical raw material.[19] New methods of incorporating H_2-inhibiting elements are then necessary. During the charging cycle of iron−air batteries (or in general in aqueous electrochemical devices dealing with HER), hydrogen is formed on the surface of the iron particles; therefore it is highly desirable to obtain an iron electroactive material with a proper distribution of the H_2-inhibiting elements.

Recently, Shangguan et al.[20] showed that adding sublimated sulfur to an Fe_3O_4 oxide in a ball mill also helps to prevent passivation by giving a supply of sulfide ions to the electrolyte and by forming pores in the electrode when dissolving. In line with this work, we propose the use of sulfur-modified iron oxides as electroactive material for iron−air batteries. Sulfur-doped or S-modified iron oxides based on hematite have been widely used as Fenton catalysts, since hematite is easily doped with heteroatoms. In the present work, we show a facile method to obtain highly pure sulfur-modified iron oxides as electroactive material for the negative electrode of an iron−air battery. The synthesis method employed herein ensures that sulfur gets introduced in the iron oxide structure, reaching an intimate and optimized distribution of sulfur on the electroactive materials,[21] with the aim of increasing the HER-suppressing effect and inhibiting passivation. Besides, the synthesis is optimized to obtain mesoporous iron oxides able

to cope with the change of volume of the electrodes during cycling, 272% molar volume increase from Fe to $Fe(OH)_2$.[22] The novelty of the present research lies in the combination of properties within one material able to tackle the three main drawbacks of iron electrodes: HER, passivation, and volume changes. These features are correlated to the discharge capacity of the iron anodes, and in fact, a model relating the discharge capacity and the number of cycles for each electrode is also presented. Operation variables such as charge and discharge rate are also investigated to elucidate the conditions that could maximize the performance of the system.

2. MATERIALS AND METHODS

2.1. Materials Synthesis. Porous sulfur-modified iron oxides were synthesized following the method presented by Du et al.[23] Oxalic acid dihydrate ($C_2H_4O_4 \cdot 2H_2O$, 0.04 mol) was dissolved in 100 mL of deionized (DI) water and heated up to 50 °C under vigorous stirring. Another solution containing 0.04 mol of iron(II) sulfate heptahydrate ($FeSO_4 \cdot 7H_2O$) and 0.02 mol of sodium thiosulfate ($Na_2S_2O_3$) in 100 mL of DI water at room temperature was prepared and added drop by drop to the first solution, maintaining the temperature at 50 °C. A yellow precipitate formed that after cooling down was filtered, washed with abundant DI water, and dried overnight at 75 °C. Iron oxides obtained from oxalic acid were named as S-Fe_2O_3-OXL. Iron oxides without sulfur (named as Fe_2O_3-OXL) were also synthesized for the sake of comparison, following the same procedure previously described without the addition of sodium thiosulfate. Another iron oxide using sodium hydroxide (NaOH) instead of oxalate as precipitating agent (named as S-Fe_2O_3-SHX) was also prepared. In this case, 0.04 mol of iron(II) sulfate heptahydrate ($FeSO_4 \cdot 7H_2O$) and 0.02 mol of sodium thiosulfate ($Na_2S_2O_3$) were dissolved in 100 mL of DI water at room temperature. Subsequently, 80 mL of NaOH 1.0 mol/L was added under vigorous stirring, drop-by-drop. The black precipitate that formed was filtered and washed with DI water and dried overnight at 75 °C. All the samples were calcined in air at 350 °C for 1 h. Subsequently, the so obtained iron oxides were mixed with Vulcan XC-72R carbon black (1:1 mass ratio) in a planetary ball mill at 100 rpm for 2 h, using ethanol 96% vol as dispersing agent. Afterward, samples were dried in an oven at 75 °C. Carbon is needed in iron electrodes to provide electrical conductivity and to maximize the utilization of the iron material. A commercial iron oxide (III) nanopowder (<50 nm, Sigma-Aldrich, named as Fe_2O_3-COM) was also studied and mixed with Vulcan for the sake of comparison.

2.2. Materials Characterization. The textural properties of the iron oxides were investigated through nitrogen physisorption at 76 K in a Micromeritics ASAP 2020. The specific surface area was determined by the Brunauer−Emmet−Teller (BET) equation, whereas the single-point and the Barrett−Joyner−Halenda (BJH) methods were used to calculate the pore volume and the average pore size, respectively. An ESCA Plus Omicron spectrometer (Scienta Omicron) with a Mg (1253.6 eV) anode setup was employed to perform X-ray photoelectron spectroscopy (XPS) studies. C 1s, O 1s, S 2p, and Fe 2p orbital signals were obtained with a step of 0.1 eV step, a dwell time of 0.5 s, and 20 eV pass energy. The quantification of orbital signals and data analysis were curated using CasaXPS software (Casa Software Ltd., CasaXPS version 2.3.18). The baseline for the different peaks was estimated through a Shirley background subtraction, and the signals were fitted with 70% Gaussian/30% Lorentzian peaks. The carbon and sulfur content of the samples was determined by elemental analysis (EA) in a Thermo Flash 1112 analyzer (Thermoscientific Waltham). A Bruker AXS D8 Advance diffractometer (Bruker) with a $\theta-\theta$ configuration and a Ru2500 diffractometer (RIGAKU) with rotating anode and $\theta-2\theta$ configuration, both using Cu Kα radiation, were employed to investigate the crystalline structure of the iron oxides using X-ray diffraction (XRD). The crystallite size of the different phases was calculated applying Scherrer's equation to the iron oxide peaks. The iron amount was

Table 1. Chemical Composition of the Sulfur-Modified Iron Oxides Determined by Elemental Analyses (EA), ICP, and XPS

material	elemental analysis, sulfur		ICP, iron		S/Fe atomic ratio (calculated from EA and ICP measurements)	XPS, atom %	
	wt %	atom %	wt %	atom %		iron	sulfur
S-Fe$_2$O$_3$-OXL	4.6	4.0	56	27.8	0.14	21.9	6.9
S-Fe$_2$O$_3$-SHX	6.6	5.5	51	24.2	0.23	18.0	4.8
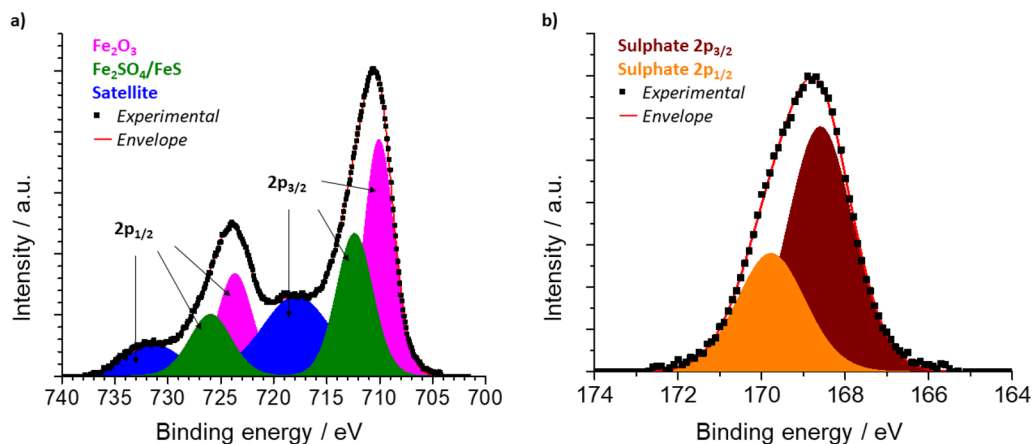
Figure 1. High-resolution XPS spectra of (a) Fe 2p orbital and (b) S 2p orbital in S-Fe$_2$O$_3$-OXL.

determined by inductively coupled plasma atomic emission spectroscopy (ICP-AES) using a Jobin Ybon 2000 spectrometer. The sample was previously fused using sodium peroxide. Each sample was measured twice, the average value being presented. The morphology of the iron oxides was investigated with a scanning electron microscope (SEM), model Hitachi S-3400N. Combining SEM with energy dispersive X-ray spectroscopy (SEM-EDX) allowed us to determine the dispersion of iron and sulfur in the composites. The equipment used was an EDX Röntec XFlash analyzer of Si(Li). FTIR analysis were performed in a Vertex 70 spectrophotometer (Bruker). The analyses were performed in the middle infrared region (from 4000 to 400 cm^{-1}) recording 32 scans at 4 cm^{-1} spectral resolution. KBr-matrix pellets were made to carry out transmittance analysis. To prepare the pellets, 2 mg of sample was mixed with 200 mg of dry KBr (>99% FTIR grade, Sigma-Aldrich), milled in an agate mortar, and pressed. Mössbauer spectroscopy (MS) data were acquired at room temperature using a constant acceleration spectrometer with symmetrical waveform and a 25 mCi ^{57}Co/Rh source. The spectrometer was calibrated at room temperature with α-Fe foil, and isomer shift values are given with respect to α-Fe.

2.3. Electrode Preparation. Iron electrodes were prepared by hot-pressing the obtained Fe$_2$O$_3$/C composites. A paste, prepared with 100 mg of the Fe$_2$O$_3$/C composite, 14 mg of PTFE (60% wt PTFE dispersion in water), and some drops of DI water, was placed within two stainless-steel meshes (2.5 cm × 7.5 cm) and hot-pressed at 25 kN and 140 °C for 90 s. The iron percentage in the electrodes ranged between 28 and 35% wt, depending on the composition of each oxide.

2.4. Electrochemical Setup and Cycling Procedures. The electrodes were tested in a conventional three-electrode cell, using a 6.0 M KOH solution as electrolyte (prepared from highly pure KOH, Alfa-Aesar-99.98% (metals basis), 85% min), a Ni sheet as counter electrode, and a Hg|HgO reference electrode, as in previous works.[15,24] To minimize the electrolyte overpotential, the working electrode and the counter electrode were placed in a holder where they faced each other separated by 0.5 cm (Figure S1). The electrodes were submitted to repeated galvanostatic charge and discharge cycles at a charge rate of 0.4 C and a discharge rate of 0.2 C, according to the theoretical capacity of the electrodes. The current (I) for each electrode and C-rate was calculated from eq 1, assuming 1273 mA h g$_{Fe}^{-1}$ as the theoretical capacity of iron (two discharge steps considered):

$$I = m_{Fe}[g] \cdot 1273 \left[\frac{mAh}{g} \right] \cdot (C - \text{rate})[h^{-1}] \tag{1}$$

3. RESULTS AND DISCUSSION

3.1. Physical−Chemical Characterization. *3.1.1. Chemical Composition.* The elemental analysis (EA) of the iron oxides (prior to the ball-milling mixing with Vulcan) (Table 1) shows that the sulfur content is 4.6 wt % for the S-Fe$_2$O$_3$-OXL and 6.6 wt % for the S-Fe$_2$O$_3$-SHX according to the EA analysis, and 6.9 atom % for S-Fe$_2$O$_3$-OXL and 4.8 atom % S-Fe$_2$O$_3$-SHX according to the XPS, meaning that S-Fe$_2$O$_3$-OXL has a S-enriched surface. The amount of sulfur in the composite is around 2.3 and 3.3 wt % in S-Fe$_2$O$_3$-OXL/C and S-Fe$_2$O$_3$-SHX/C, respectively. In the literature, the amount of sulfur used as an additive in the negative electrode ranges between 0.2 wt % as bismuth sulfide[15,25,26] and 2 wt % as iron sulfide.[14,27] Deng et al.[21] determined by DFT calculations that hematite iron oxides synthesized from ferrous sulfate and sodium thiosulfate mixtures (as in the present work) can be doped with sulfur, as is the case of our iron oxides, by two mechanisms: either interstitial or with sulfur replacing O atom in the crystalline structure of hematite. The amount of iron was also calculated by both XPS and ICP to estimate the ratio of S/Fe (also shown in Table 1). The weight % of iron is similar for both materials, around 50 wt %, equivalent to around 25 atom %. This means that S-Fe$_2$O$_3$-OXL presents a S/Fe ratio of 0.14 with respect to the S-Fe$_2$O$_3$-SHX with a S/Fe ratio of 0.23.

High-resolution XPS spectra of the Fe 2p orbital reveals that iron is mostly present as iron(III) oxide (Figure 1a), even though other forms of iron oxides or hydroxides might be present. The deconvolution of the iron spectrum curve of S-Fe$_2$O$_3$-OXL shows three Fe 2p$_{3/2}$ peaks, at 710.9, 712.6, and 718.9 eV, which are ascribed to iron sulfate or sulfide, iron(III) oxide, and the classic satellite peak of Fe$_2$O$_3$ 2p$_{3/2}$, respectively;[23,28] in samples without sulfur, only peaks related

to Fe_2O_3 can be seen (Figure S2). Due to the proximity of the characteristic binding energies of iron sulfate and iron sulfide (FeS) in the high-resolution iron XPS spectrum,[29] it is hard to distinguish among these two species. The observation and analysis of the sulfur orbital help to elucidate this ambiguity (Figure 1b). The main $2p_{3/2}$ peak is observed at 168.7 eV, which should correspond to sulfate.[28,30,31] The absence of peaks at lower binding energies (see Figure S2e) (mackinawite and pyrite show sulfur peaks at around 162 eV [32]) allows us to dismiss the presence of sulfides. Using oxalate as precipitating agent during the synthesis entails a more acidic pH (approximately 4−5) that eventually favors the adsorption of sulfate groups on the surface.[33]

3.1.2. Crystallographic Structure: Mössbauer Spectroscopy and X-ray Diffraction.
The phases present in the samples were determined by XRD (Figure S3), FTIR (Figure S4), and Mossbauer spectroscopy (Figure 2). The room temperature
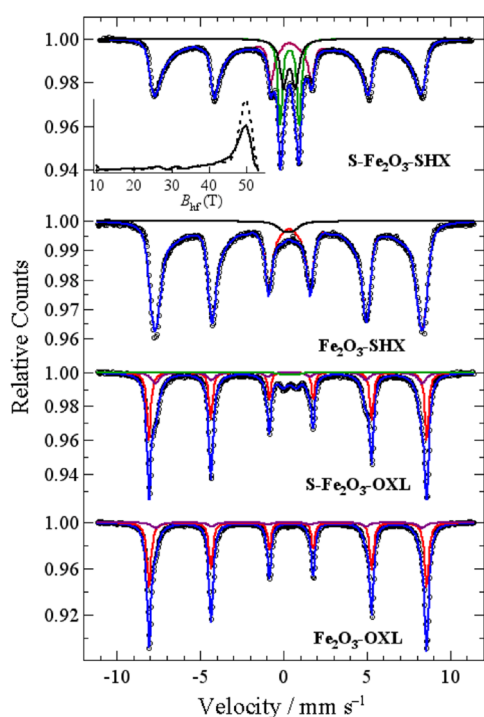

Figure 2. Mössbauer spectra of samples Fe_2O_3-OXL, S-Fe_2O_3-OXL, Fe_2O_3-SHX, and S-Fe_2O_3-SHX. For the SHX samples, the distribution of hyperfine field values is shown in the inset (dotted line, Fe_2O_3-SHX; full line, S-Fe_2O_3-SHX).

Mössbauer spectra of the oxides obtained by precipitation with oxalic acid (named as OXL) or sodium hydroxide (named as SHX) are shown in Figure 2 along with the spectra of the corresponding sulfur modified samples. The spectrum of Fe_2O_3-OXL was fitted with two sextets, while for the sulfur

modified sample S-Fe_2O_3-SHX a doublet was added (Table S1). The sextets are straightforwardly (columns marked with S1 and S2 in Table S1 in Supporting Information) assigned to hematite and maghemite, respectively, according to their hyperfine parameters, while the intensity at the center of the S-Fe_2O_3-OXL spectrum, modeled as small doublet of very broad peaks, can be assigned to a paramagnetic Fe^{3+} compound because of its isomer shift value. In contrast, the samples prepared with NaOH do not display neat sextets but broad peaks which are asymmetric toward the center of the spectrum. This is an indication of a distribution of particle size including very small particles with superparamagnetic behavior at room temperature, which can also be observed in the XRD patterns (Figure S3). In this case, the spectra were fitted with a distribution of sextets and a broad central doublet to account for the iron oxides and their superparamagnetic behavior of very small particles, while the distribution of sextets and two doublets was used in the spectrum of the sulfur modified sample. In S-Fe_2O_3-OXL the isomer shift and quadrupole splitting values of the doublets are consistent with $Fe_2(SO_4)_3 \cdot 5H_2O$;[34] however, the relative areas of the doublets do not match those of pure $Fe_2(SO_4)_3 \cdot 5H_2O$,[34] with an extra intensity in the inner (lowest quadrupole splitting) doublet, which may be assigned to the superparamagnetic contribution of iron oxides. Using the spectral area of the outer (largest quadrupole splitting) doublet as pure $Fe_2(SO_4)_3 \cdot 5H_2O$, we can estimate a sulfur to iron atomic ratio of $\frac{3}{2}15.5 \approx 23\%$, in good agreement with the results of AE and ICP of 22.7% (Table 1).

The relative areas of the hematite and maghemite sextets in the samples prepared with oxalic acid show that maghemite formation is promoted when sodium thiosulfate is used to introduce sulfur, and Fe^{3+} sulfates still unidentified are formed at the expense of the hematite yield. The process is similar in the samples prepared with NaOH, as it can be observed by the decrease in the contribution of the largest hyperfine field values (Figure 2, inset) associated with hematite, but in this case the production of a Fe^{3+} sulfate, identified as $Fe_2(SO_4)_3 \cdot 5H_2O$, is much higher.

The synthesis method has a clear effect on the crystal structure: the oxides obtained by precipitation with oxalic acid (OXL) consist of mixtures of well crystallized hematite and maghemite, whereas the one obtained by precipitation with sodium hydroxide (SHX) shows broad reflections, especially those that can be assigned to hematite; e.g., note reflection (1 0 4) at $2\theta \approx 33°$ (Figure S3 in Supporting Information). Table 2 shows the approximate proportion of each phase in our iron oxides determined by MS and Rietveld profile fits using the FullProf code,[35] and average crystal size was obtained by Scherrer's equation. The fits included the refinement of the occupancy of one of the octahedral sites in maghemite;[36] in both cases the refined occupancy indicated close to stoichiometric maghemite. The profile of the diffractogram of

Table 2. Crystalline Phases and Average Crystal Size of the Different Iron Oxides

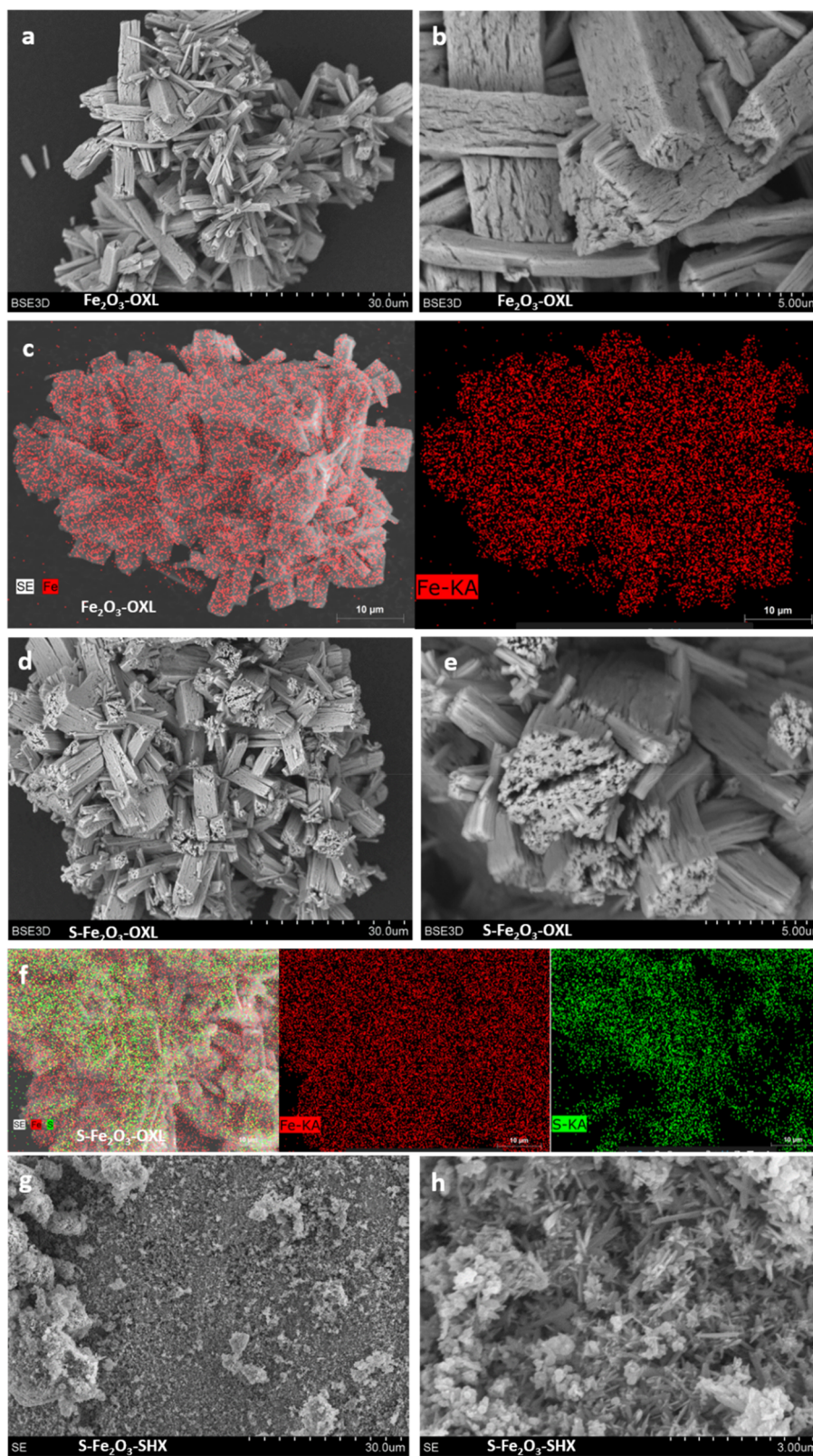| material	crystal phase, %		average crystallite size, nm		from sextet areas in MS, %	
	hematite	maghemite	hematite	maghemite	hematite	maghemite
Fe_2O_3-COM		100		20		
Fe_2O_3-OXL	79	21	17	17	76.1	23.9
S-Fe_2O_3-OXL	65	35	14	19	56.4	43.6
S-Fe_2O_3-SHX			8	4		

D

Figure 3. continued

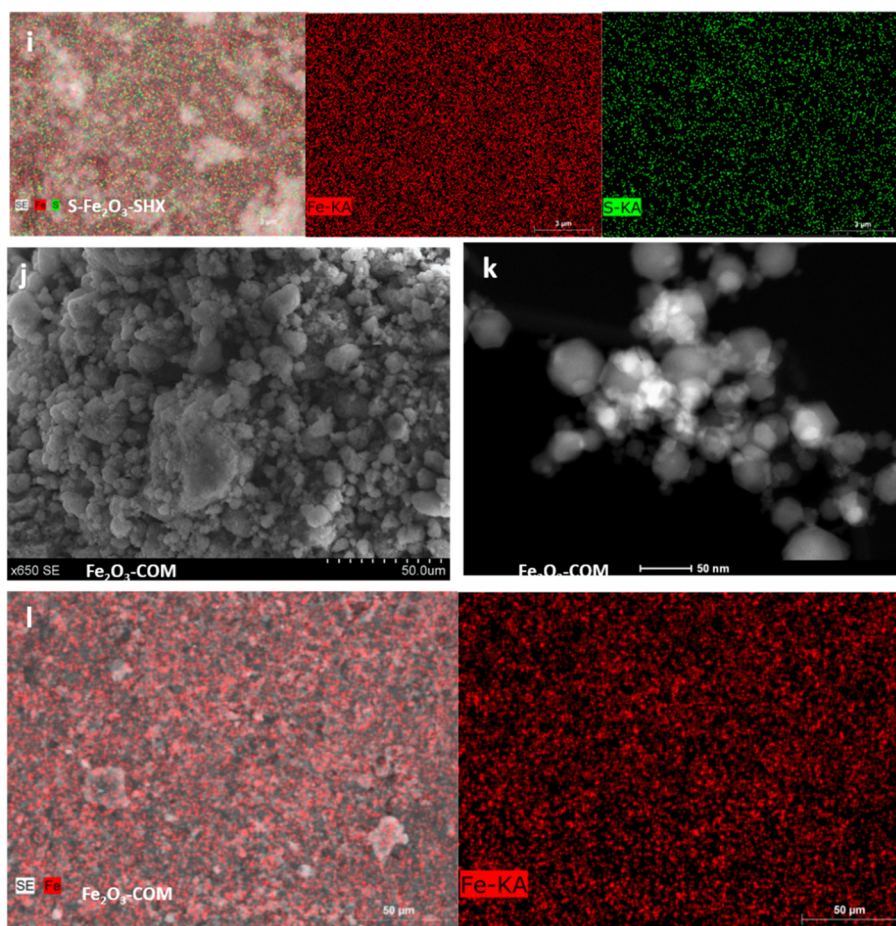**Figure 3.** Micrographs at low (left) and high (right) magnification and EDX mapping for (a−c) Fe_2O_3-OXL, (d−f) S-Fe_2O_3-OXL, (g−i) S-Fe_2O_3-SHX, (j−l) Fe_2O_3-COM.

S-Fe_2O_3-SHX could not be fitted properly; hence no phase proportion is provided from these data and the crystallite size can only be estimated as 4−8 nm from the average width of some reflections.

According to previous studies, maghemite transition to hematite starts at around 320 °C for pure iron oxides and around 450 °C and at low rates for iron oxides with impurities,[37] which is a sign that impurities (such as sulfur, in this case) stabilize maghemite and, hence, promote its formation. Also, previous works show that hematite is obtained when calcining hydrated iron oxalates in air at around 400 °C.[38] In the present study, sulfur seems to promote the formation of maghemite upon iron oxalate calcination, as can be inferred from the fact that S-Fe_2O_3-OXL has a lower fraction of hematite than Fe_2O_3-OXL, as was also observed by MS. In addition, it has been reported that hematite is obtained from hydrothermal treatment of $FeSO_4$ with bases.[39]

The average crystal sizes (calculated from Scherrer's formula) are between 4 and 20 nm (Table 2). Fe_2O_3-COM, Fe_2O_3-OXL, and S-Fe_2O_3-OXL, have similar average crystal size, whereas for S-Fe_2O_3-SHX crystal size is considerably lower. The small size of particles and large area are also important to provide good contact between the carbon and the metal oxide phase, which is crucial to reduce the ohmic overpotential. Like what is observed in XPS, no sulfide crystal phases are observed in XRD. However, some peaks are appreciated which could correspond to sulfate phases (green marks in Figure S3). This is another evidence suggesting that

there is no sulfide in the samples and that all the sulfur is in the form of sulfate groups.

Figure S4a,b in the Supporting Information shows the FTIR spectra for the different iron oxides, evidencing notorious differences between samples. FTIR results confirm XRD identification of phases (Figure S4). Besides, for the sulfur modified sample obtained from oxalic acid, the FTIR analysis reveals the presence of adsorbed sulfate groups, which is in concordance with the greater amount of sulfur observed in the surface of this sample by XPS. Gotic et al.[33] also described the presence of adsorbed sulfates on iron oxides obtained at acidic pH values, as is the case for S-Fe_2O_3-OXL.

3.1.3. Textural Properties. All the iron oxides show a type-IV adsorption−desorption isotherm (see Figure S5 in the Supporting Information), characteristic of mesoporous materials, and surface areas between 30 and 55 m^2/g (see Table S2), with porosity values around 50% and large mesopores (~15 nm) that may help accommodate the volume changes of the electrodes upon cycling.

3.1.4. Morphology. Figure 3 shows the SEM micrographs at different magnifications. Both Fe_2O_3-OXL (Figure 3a and Figure 3b) and S-Fe_2O_3-OXL (Figure 3d and Figure 3e) consist of agglomerates of parallelepipeds of around 5 μm of average transversal length made of iron oxide crystallites. These structures show irregularities (Figure 3a−f), cracks, and fissures, which are formed during the thermal decomposition of oxalate ions.[23] Iron oxide S-Fe_2O_3-SHX has a completely different morphology. At low magnifications (Figure 3g) it

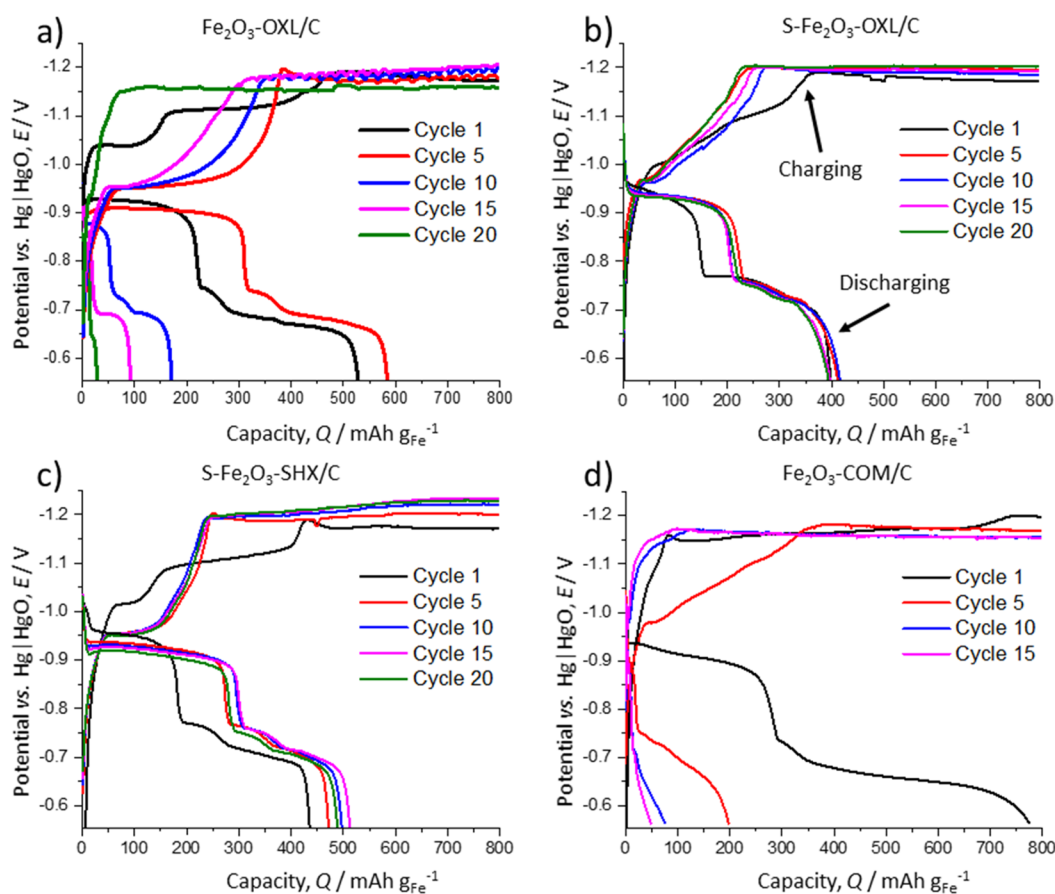**Figure 4.** Charge−discharge cycles of the electrodes manufactured with (a) Fe_2O_3-OXL/C, (b) S- Fe_2O_3-OXL/C, (c) S- Fe_2O_3-SHX/C, and (d) Fe_2O_3-COM/C. Charge rate, 0.4 C; discharge rate, 0.2 C.

looks like a compact irregular material, while zooming in Figure 3h lets us appreciate a mixture of ball-like and needle-like shape of the particles. The mesoporosity observed for this material is a consequence of the spaces between these small structures. The SEM image of Fe_2O_3-COM, Figure 3j, shows it has a blackberry-like morphology, consisting of aggregates of thousands of smaller particles. The STEM image (Figure 3k) shows that this material is composed of nanometric regular polyhedron particles. According to the manufacturer, the maximum diameter of these particles is 50 nm. Indeed, it can be observed that the size of the Fe_2O_3 particles ranges from approximately 10 to 50 nm.

EDX mapping was performed to evaluate the distribution of both iron and sulfur on the obtained materials. Fe_2O_3-OXL (Figure 3c) and Fe_2O_3-COM (Figure 3l) present a homogeneous distribution of iron, without any trace of sulfur, whereas S-Fe_2O_3-OXL (Figure 3f) and S-Fe_2O_3-SHX (Figure 3i) present a proper distribution of both iron and sulfur. This means that the sulfur present in the sulfur-modified materials comes from the thiosulfate added in the synthesis and not from the iron(II) sulfate employed as iron precursor. As can be seen in Figure 3f and Figure 3i, sulfur is well dispersed over the iron particles, suggesting a homogeneous mixture between iron oxide and sulfate phases or sulfur species adsorbed over the entire iron oxide surface. Additionally, STEM-EDS analyses were carried out to corroborate that sulfur was present along all of the iron particles. Indeed, as seen in Figure S6, there is presence of sulfur in every iron crystallite, in both S-Fe_2O_3-OXL and S-Fe_2O_3-SHX.

3.2. Electrochemical Characterization. *3.2.1. Discharge Capacities.* The four materials were characterized in a three-electrode cell to determine their discharge capacities and test their stability. The charge−discharge potentiometric curves are shown in Figure 4. A total of 20 cycles (between 70 and 100 h) were performed. Figure 4 indicates the differences in stability for the assessed electrodes, the sulfur-modified iron oxides (S-Fe_2O_3-OXL/C and S-Fe_2O_3-SHX/C) being the most stable ones, which will be deeply discussed in the following section.

During the discharge, a first plateau can be observed at −0.94 V vs Hg|HgO, corresponding to the oxidation of metallic iron to iron(II) hydroxide. As metallic iron, an excellent electrical conductor is oxidized to $Fe(OH)_2$, which is an insulator, the resistance of the system increases, and so the potential reaches more negative values. Studies have shown that the oxidation of metallic iron to iron(II) hydroxide occurs through a dissolved intermediate, $HFeO_2^-$, which then precipitates as crystallite particles, increasing the surface roughness.[40−43] When all the crystallization sites are covered (at low overpotential), an insulating layer is formed. When all the remaining iron atoms are covered by the insulating layer, the overpotential increases and the inner atoms oxidize at potentials where the second discharge step also occurs. The second discharge plateau can be divided into two smaller plateaus, suggesting the second discharge step is composed by two reactions: the oxidation of iron(II) hydroxide to magnetite, and then the oxidation of magnetite to iron(III) oxyhydroxide, as can be inferred from the post-mortem XRD analysis (Figure S7).

Figure 5 shows the maximum discharge capacity (black bar) reached by the different iron anodes tested during 20 cycles,
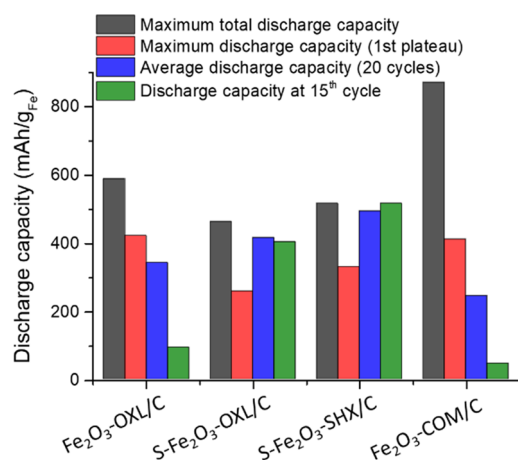

Figure 5. Discharge capacity values for each material: max = best discharge capacity of all cycles; 15th cycle = discharge capacity at 15th cycle; max first step = maximum discharge capacity at −0.75 V vs Hg|HgO. Charge rate: 0.4 C. Discharge rate: 0.2 C.

along with the maximum discharge capacity obtained at the first plateau (after the first oxidation reaction, from Fe to Fe(OH)$_2$,) at approximately −0.75 V vs Hg|HgO (blue bar). This value is of interest for the practical application of these electrodes, as the first discharge plateau provides more energy

due to its higher electrochemical potential. Figure 5 also presents the average discharge capacity (medium value considering the 20 charge−discharge cycles) and the discharge capacity at the 15th cycle (red bar); these data will be important in the next section. The electrode with the highest capacity, the one prepared with commercial iron(III) oxide nanoparticles, reaches a maximum discharge capacity of 881 mA h g$_{Fe}^{-1}$, which is almost 70% of the theoretical capacity (considering both discharge steps), that however is not sustained with time (capacity decays to 40 mA h g$_{Fe}^{-1}$ in the 15th cycle). On the other hand, the two composites based on sulfur-modified iron oxides show a maximum capacity ranging from 450 to 500 mA h g$_{Fe}^{-1}$ (superior to current lithium ion-batteries) and a higher stability, retaining most of their maximum capacity. Iron oxides obtained with either oxalic acid (OXL) or sodium hydroxide (SHX) present capacity values at the first plateau from 250 to 420 mA h g$_{Fe}^{-1}$, in comparison to the commercial composite reaching as high as 400 mA h g$_{Fe}^{-1}$, but it is not sustained during cycling. In terms of Coulombic efficiencies, the best value is achieved by Fe$_2$O$_3$-COM/C, with almost 70% as a maximum, whereas Fe$_2$O$_3$-OXL/C shows a sustained 50%.

It is interesting to note that the maximum capacity of the electrodes is not correlated to the surface area or the crystal size of the iron oxides, which is a consequence of the described dissolution−precipitation reaction mechanism; the dissolution of HFeO$_2^-$ exposes new iron atoms that are then oxidized, as was explained above. In fact, Fe$_2$O$_3$-COM/C has the highest maximum discharge capacity and the second-to-lowest surface
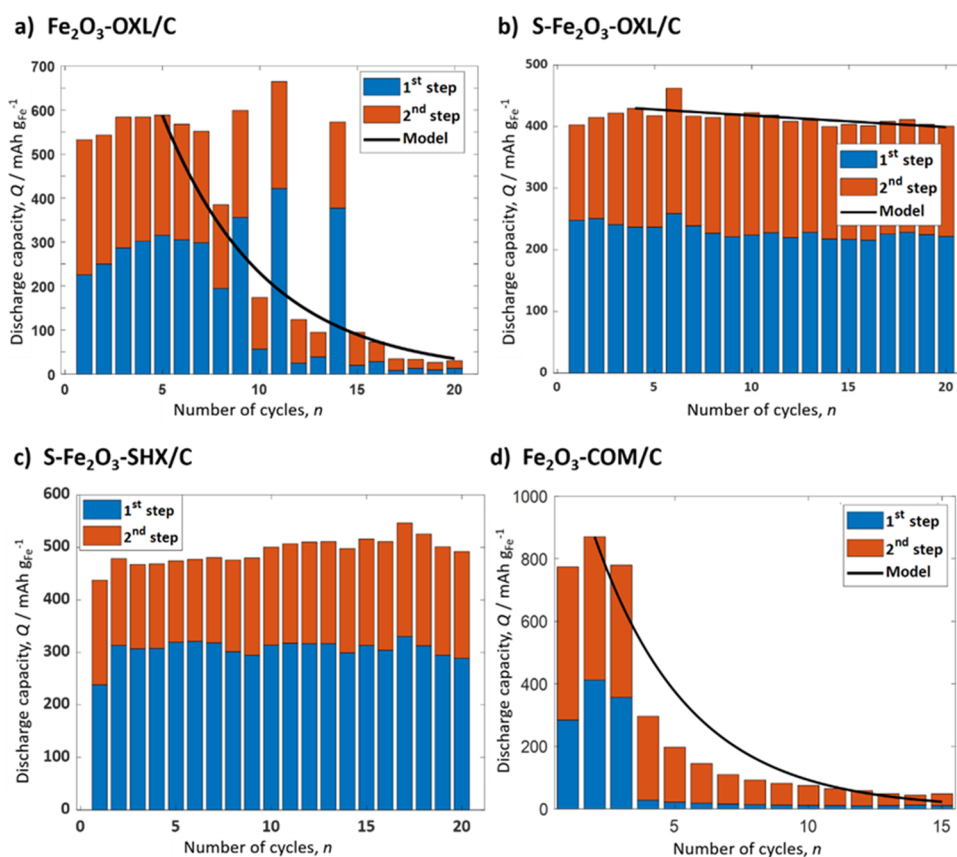

Figure 6. Discharge capacity values for each cycle for the electrodes manufactured with composites (a) Fe$_2$O$_3$-OXL/C, (b) S-Fe$_2$O$_3$-OXL/C, (c) S-Fe$_2$O$_3$-SHX/C, and (d) Fe$_2$O$_3$-COM/C. Charge rate: 0.4 C. Discharge rate: 0.2 C. Black line corresponds to the model adjusting the capacity fading with the cycles.

area of all the samples (Table S2), showing similar crystal sizes when compared to iron oxides obtained from oxalate precipitation (Table 2). The crystalline phases also do not behave as reported by Lee et al.,[44] with S-Fe$_2$O$_3$-OXL/C showing a much more stable performance than Fe$_2$O$_3$-OXL/C, even though they are composed of 44% and 24% maghemite, respectively (Table 2). In fact, in the cited article, maghemite electrodes do not reach capacities higher than 80 mA h g$_{Fe}^{-1}$, while in the present work the 100% maghemite electrode achieves more than 10 times that amount, although for only three cycles.

3.2.2. Stability of the Electrodes. Another information obtained from the charge−discharge cycles was the mid-term stability in operation, i.e., how fast the discharge capacity was lost during repeated cycling. Figure 6 shows that as the electrode charges and discharges, the discharge capacity increases for the first cycles, which is known as the formation period. In carbonyl−iron electrodes, the formation period can last from 20 up to 200 cycles,[22,24,26,45] while in nanometric iron oxide electrodes it can take only a few cycles or even none,[24,46] as is the case of our electrodes. The authors attribute this to the combination of sufficient surface area and small particle size of our iron oxides. After the formation period, the discharge capacity slowly decreases but not at the same rate for all materials. Both Fe$_2$O$_3$-OXL/C (Figure 6a) and Fe$_2$O$_3$-COM/C (Figure 6d), the latter with the highest maximum discharge capacity, quickly deactivate and lose capacity upon cycling. On the other hand, sulfur-modified iron oxides, namely, S-Fe$_2$O$_3$-OXL/C (Figure 6b) and S-Fe$_2$O$_3$-SHX/C (Figure 6c), present a very stable behavior upon cycling, barely losing discharge capacity with time. To elucidate the mechanism of deactivation and compare the different iron−carbon composites, a mathematical model was developed and adjusted to the capacity of the composites over the cycles. A full description can be found in the Supporting Information. The black line corresponds to the model adjusting the capacity fading with the cycles, which will be discussed ahead.

The mechanism by which the iron electrodes deactivate is still under discussion. Most authors propose that deactivation is due to the passivation of the electrode, i.e., the repetitive formation and dissolution of an insulating layer of Fe(OH)$_2$ over the iron atoms.[47−49] When this layer reaches certain thickness, due to the inefficiency of the dissolution (charge process), the resistance increases and subsequently so does the overpotential, up to the limit where it is practically impossible to reduce the iron(II) hydroxide to iron at reasonable working potentials. Another hypothesis for the loss of capacity of iron electrodes regards the plugging of the pores[47] (which also causes an ohmic loss of potential) and the loss of electroactive material. The plugging effect is significant mainly because of the increase in molar volume during the discharge, as the oxidation products of iron are much less dense than metallic iron. The volume change of iron after discharging can be clearly observed by SEM in Figure S8, showing an increase of the size of the iron oxide particles upon cycling. The hypothesis of material loss during the cycling was studied by Kitamura et al.[50] and by Figueredo-Rodríguez et al.,[16] who observed a structural change in the iron particles after 20 cycles and also some damage due to gas evolution. During our experiments, we were able to see that material dropped from the electrode into the electrolyte and settled at the bottom of the cell. This effect was stronger in the electrodes manufactured with nonmodified iron oxide and could be

caused by mechanical stress applied by hydrogen bubbles formed within the electrode, which indicates the importance of a proper distribution of the inhibiting HER elements within the structure of the electrode

To elucidate the mechanism of deactivation and compare the different iron−carbon composites, a mathematical model was developed and adjusted to the capacity of the composites over the cycles. A full description can be found in the Supporting Information. The assumptions made for this model, described in eq 2, were the following: (i) the electrodes take a few cycles to activate, in which their capacity increases, and after that, (ii) the capacity decreases exponentially down to zero after infinite cycles.

$$Q = Q_i \cdot f^{n-i} \qquad (2)$$

where Q is the discharge capacity of the electrode at a cycle n, i is the number of the first cycle after activation, Q_i is the discharge capacity of the electrode in that cycle, and f is a factor that indicates how ideally the electrode works or how fast it deactivates. In an electrode that does not lose capacity at all, f would be equal to 1 ($f = 1$). The electrode manufactured with Fe$_2$O$_3$-OXL/C (Figure 6a) needs four cycles to activate, while S- Fe$_2$O$_3$-OXL/C (Figure 6b) needs three. After that, the discharge capacity of Fe$_2$O$_3$-OXL/C (Figure 6a) rapidly decreases, almost monotonically, except for the 9, 11, and 14 cycles, where a sharp but not sustained increase in the capacity is observed. The most plausible explanation for this phenomenon is that hydrogen bubbles delaminate the electrode and break the material, creating new pores and exposing new active surface. Nevertheless, those pores are quickly plugged again by inactive material. In this case, we believe that both passivation and plugging of the pores take place at the same time, which would sustain the previous explanation. The f factor calculated for this electrode is 0.829.

The electrode manufactured with the S-Fe$_2$O$_3$-OXL/C composite shows a very steady behavior (Figure 6b). From cycle 4 and on, the discharge capacity slowly decreases at a pace less than 0.5%/cycle ($f = 0.995$). Comparing the properties of Fe$_2$O$_3$-OXL/C and S-Fe$_2$O$_3$-OXL/C, the two oxides used for these composites present close values of surface area, porosity, pore size, and crystal size. The only differences are the absence or presence of sulfur and the ratio of maghemite to hematite. Nevertheless, the Fe$_2$O$_3$-COM/C composite is exclusively formed by maghemite and has a very poor performance in terms of stability (Figure 6d), so the most plausible explanation is that sulfur is indeed preventing passivation in S-Fe$_2$O$_3$-OXL/C.

For the two other composites (S-Fe$_2$O$_3$-SHX/C, Figure 6c and Fe$_2$O$_3$-COM/C, Figure 6d), the proposed model does not fit the data as well as it does with the oxalate-based iron oxide composites. S-Fe$_2$O$_3$-SHX/C (Figure 6c) shows a different behavior. During the first 20 cycles, the tendency is that its capacity increases, indicating that the material is still not fully activated. This behavior will be deeply discussed in the next section. However, both S-Fe$_2$O$_3$-SHX/C and S-Fe$_2$O$_3$-OXL/C, present a more stable performance than the electrodes that did not contain sulfur.

For the Fe$_2$O$_3$-COM/C electrode (Figure 6d), the first three cycles have an exceptionally high discharge capacity, which immediately decays to less than half in the following cycles. As seen in Table S2, the oxide in which this composite is based has the lowest surface area and porosity of all, which makes it prone to pore plugging. As the cycling advances, the electrode

loses capacity especially in the first discharge plateau. This is a signal that iron hydroxide is not reducing to metallic iron, which supports the hypothesis of passivation by insulating layer.

According to several studies,[14,51,52] sulfur prevents passivation of iron electrodes when present as iron sulfide or bismuth sulfide. Some new studies have shown that adding elemental sulfur to the electrodes can have a strong impact in preventing passivation. As Shangguan et al. showed by XRD analysis,[20] sublimated sulfur can reduce to S^{2-}, which dissolves into the electrolyte and then is adsorbed by iron particles, forming FeS and other nonstoichiometric iron sulfides. In this case, the post-mortem XRD analysis was inconclusive (see Figure S7 in the Supporting Information), but XPS shows that, indeed, sulfate present in the fresh sulfur-modified iron oxides reduces to species that, according to the binding energies, could be S or
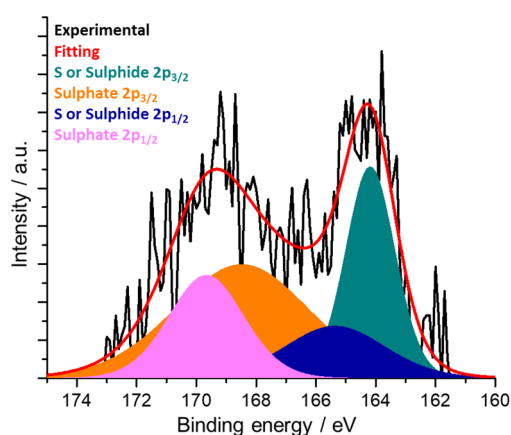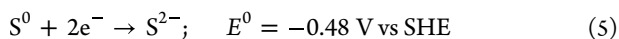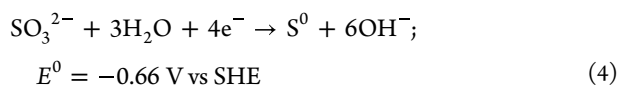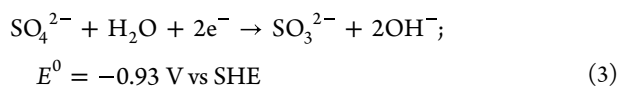

Figure 7. XPS post-mortem spectrum of the composite S-Fe_2O_3-OXL/C in the sulfur 2p orbital region.

S^{2-} (Figure 7). Equations 3−5 show the path that sulfur can follow in alkaline media to reduce from sulfate to sulfide:

$$SO_4^{2-} + H_2O + 2e^- \rightarrow SO_3^{2-} + 2OH^-;$$
$$E^0 = -0.93\ \text{V vs SHE} \tag{3}$$

$$SO_3^{2-} + 3H_2O + 4e^- \rightarrow S^0 + 6OH^-;$$
$$E^0 = -0.66\ \text{V vs SHE} \tag{4}$$

$$S^0 + 2e^- \rightarrow S^{2-}; \quad E^0 = -0.48\ \text{V vs SHE} \tag{5}$$

The reduction from sulfate to sulfite (eq 3) takes place at a more negative potential than the reduction of iron(II) hydroxide. Nevertheless, −0.93 V vs SHE is equivalent to −1.03 V vs Hg|HgO, so the standard potential for this reaction is less negative than the potentials at which the system is working. Once the sulfate is reduced to sulfite, it should rapidly reduce to sulfur and then sulfide, as the standard equilibrium potentials for these reactions (eqs 4 and 5) are much less negative than those at the working electrode. This explains why no sulfite peaks are observed in Figure 7 being highly probable that the peak at 163.9 eV corresponds to sulfide. As has been demonstrated in previous literature,[53,54] sulfide ions react with iron(II) hydroxide to form the much more conductive iron(II) sulfide and other conductive iron sulfide species.

More evidence for the passivation preventing effect of sulfur can be found in the fresh and post-mortem electrode SEM images and EDX analyses (Figure S9). It can be seen that the iron crystal agglomerates grow after 20 cycles, and this effect is more evident in electrode Fe_2O_3-COM/C than in S-Fe_2O_3-OXL/C, consistent with the higher maximum discharge capacity of the first electrode over the latter. Especially interesting are the EDX analyses of the electrodes before and after cycling. Before cycling, it can be seen that the electrode Fe_2O_3-COM/C has a high amount of oxygen in the iron particle, which means the iron is oxidized. After 20 cycles, the amount of oxygen detected by EDX is considerably lower, which is a signal that only a small amount of the iron was able to oxidize. This is consistent with the electrode being passivated by a layer of iron(II) hydroxide over the metallic particles which does not allow the bulk of them to react. In electrode S-Fe_2O_3-OXL/C, the height of the oxygen peak in the EDX scan relative to the iron peak is almost the same in the fresh electrode and in the electrode cycled 20 times, showing that the passivation of iron in this electrode is much slower.

Electrodes based on sulfur-modified iron oxides were subjected to extended cycling (60 cycles, approximately 200−280 h). Further details on these experiments can be found in the Supporting Information.

Operation variables were also investigated to elucidate the conditions that could maximize the performance of the system. Electrodes manufactured with S-Fe_2O_3-OXL/C were cycled at higher C-rates (i.e., higher charging and discharging currents). The detailed information can be found in the Supporting Information.

4. CONCLUSIONS

We prepared mesoporous sulfur-modified iron oxides, which were mixed with commercial carbon (Vulcan XC-72R) to form Fe/C composites and tested as negative electrodes for iron−air batteries. Unlike most previous negative iron electrodes, the sulfur was directly produced as a composite material with the iron rather than being added by simple physical mixing. The synthesis of the iron oxide was facile, and it could be prepared in a scalable manner at low cost. The following paragraphs will summarize the significant findings that were observed.

The discharge capacities of the iron electrodes ranged from 400 to 850 mA h g_{Fe}^{-1}; although the iron electrodes with sulfur modification had lower capacities than those without, the cycle stability was vastly improved by the addition of sulfur. The positive effect of sulfur outstrips any the effect of any other feature such as phase composition or particle size.

The oxalate-precipitated sulfur-modified iron oxide (S-Fe_2O_3-OXL) proved to be a superior material for long-term cycling. The exponential decay in the discharge capacity was much lower such that it was able to maintain 95% of its initial capacity after 20 cycles (~100 h) at 0.4 C (charge) to 0.2 C (discharge) rates. It even maintained 65% discharge capacity after 500 h of operation. In comparison, the same material prepared without sulfur almost completely deactivated after 20 cycles and commercial iron(III) oxide nanopowder deactivated after 15 cycles.

The synthesis method allowed uniform distribution of sulfur on the surface of the iron oxide. The high degree of physical contact between the iron and sulfur phases improves the electrochemical stability of the electrode by enhancing the suppression of hydrogen evolution and passivation (as demonstrated by the improved Coulombic efficiency).

The mechanism by which prevention of passivation occurs is reduction of sulfate species into sulfide under the operating conditions, which then decreases the potential for hydrogen evolution at the electrode surface area.

Finally, we demonstrated control of the charge and discharge rates to enhance different properties. Lower charge and discharge rates resulted in the operation of the electrodes being more stable (less than 0.5% capacity loss per cycle), and by increasing the rates, we could increase the Coulombic efficiency of the process from 35% up to 65%.

The results obtained from this research present a useful tool for manufacture and operation of iron electrodes in an iron–air battery. In order to achieve the highest Coulombic efficiency, a charging rate of 0.8 C and a charge time of 50 min are recommended. A lower charge rate, 0.4 C, is recommended to extend the useful life of the electrode.

■ ASSOCIATED CONTENT

ⓈⒾ Supporting Information

The Supporting Information is available free of charge at https://pubs.acs.org/doi/10.1021/acsaem.2c02123.

> Complementary physical–chemical and electrochemical characterizations; scheme and photograph of the electrochemical cell (PDF)

■ AUTHOR INFORMATION

Corresponding Authors

Cinthia Alegre − *Instituto de Carboquímica, Consejo Superior de Investigaciones Científicas, 50018 Zaragoza, Spain*; ⓞ orcid.org/0000-0003-1221-6311; Email: cinthia@icb.csic.es

María Jesús Lázaro − *Instituto de Carboquímica, Consejo Superior de Investigaciones Científicas, 50018 Zaragoza, Spain*; Email: mlazaro@icb.csic.es

Authors

Nicolás Villanueva − *Instituto de Carboquímica, Consejo Superior de Investigaciones Científicas, 50018 Zaragoza, Spain*

Javier Rubin − *Instituto de Nanociencia y Materiales de Aragón (INMA), CSIC-Universidad de Zaragoza, 50009 Zaragoza, Spain; Departamento de Ciencia y Tecnología de Materiales y Fluidos, Universidad de Zaragoza, 50018 Zaragoza, Spain*; ⓞ orcid.org/0000-0003-1029-3751

Horacio A. Figueredo-Rodríguez − *Electrochemical Engineering Laboratory, Energy Technology Research Group, Faculty of Engineering and Physical Sciences, Southampton University, Southampton SO17 1BJ, U.K.*; Present Address: Escuela de Ingeniería y Ciencias, Tecnológico de Monterrey, CCM, 14380, CDMX, México; ⓞ orcid.org/0000-0003-2892-6780

Rachel D. McKerracher − *Electrochemical Engineering Laboratory, Energy Technology Research Group, Faculty of Engineering and Physical Sciences, Southampton University, Southampton SO17 1BJ, U.K.*

Carlos Ponce de León − *Electrochemical Engineering Laboratory, Energy Technology Research Group, Faculty of Engineering and Physical Sciences, Southampton University, Southampton SO17 1BJ, U.K.*

Complete contact information is available at:
https://pubs.acs.org/10.1021/acsaem.2c02123

Author Contributions

The manuscript was written through contributions of all authors. All authors have given approval to the final version of the manuscript.

Notes

The authors declare no competing financial interest.

■ REFERENCES

(1) Masson-Delmotte, V. P.; Zhai, H.-O.; Pörtner, D.; Roberts, J.; Skea, P. R.; Shukla, A. P. W.; Moufouma-Okia, C.; Péan, R.; Pidcock, S.; Connors, J.B. R.; Matthews, Y.; Chen, X.; Zhou, M. I.; Gomis, E.; Lonnoy, T.; Maycock, M.; Tignor, T. W.Global Warming of 1.5°C. An IPCC Special Report on the Impacts of Global Warming of 1.5°C above Pre-Industrial Levels and Related Global Greenhouse Gas Emission Pathways, in the Context of Strengthening the Global Response to the Threat of Climate Change. Cambridge University Press: Cambridge, U.K., 2018; 616 pp, 2 (October); pp 17–20.

(2) Solaymani, S. CO2 Emissions Patterns in 7 Top Carbon Emitter Economies: The Case of Transport Sector. *Energy* **2019**, *168*, 989–1001.

(3) Metzler, D.; Humpe, A.; Gössling, S. Is It Time to Abolish Company Car Benefits? An Analysis of Transport Behaviour in Germany and Implications for Climate Change. *Clim. Policy* **2019**, *19* (5), 542–555.

(4) Gandoman, F. H.; Jaguemont, J.; Goutam, S.; Gopalakrishnan, R.; Firouz, Y.; Kalogiannis, T.; Omar, N.; Van Mierlo, J. Concept of Reliability and Safety Assessment of Lithium-Ion Batteries in Electric Vehicles: Basics, Progress, and Challenges. *Appl. Energy* **2019**, *251*, 113343.

(5) Li, M.; Lu, J.; Chen, Z.; Amine, K. 30 Years of Lithium-Ion Batteries. *Adv. Mater.* **2018**, *30* (33), 1800561.

(6) Balakrishnan, P. G.; Ramesh, R.; Prem Kumar, T. Safety Mechanisms in Lithium-Ion Batteries. *J. Power Sources* **2006**, *155* (2), 401–414.

(7) Wang, C.; Yu, Y.; Niu, J.; Liu, Y.; Bridges, D.; Liu, X.; Pooran, J.; Zhang, Y.; Hu, A. Recent Progress of Metal-Air Batteries-A Mini Review. *Appl. Sci.* **2019**, *9* (14), 2787.

(8) Yaroshevsky, A. A. Abundances of Chemical Elements in the Earth's Crust. *Geochemistry Int.* **2006**, *44* (1), 48–55.

(9) Weinrich, H.; Durmus, Y. E.; Tempel, H.; Kungl, H.; Eichel, R.-A. A. Silicon and Iron as Resource-Efficient Anode Materials for Ambient-Temperature Metal-Air Batteries: A Review. *Materials* **2019**, *12* (13), 2134.

(10) McKerracher, R. D.; Ponce de Leon, C.; Wills, R. G. A.; Shah, A. A.; Walsh, F. C. A Review of the Iron-Air Secondary Battery for Energy Storage. *ChemPlusChem* **2015**, *80* (2), 323–335.

(11) Malkhandi, S.; Yang, B.; Manohar, A. K.; Prakash, G. K. S.; Narayanan, S. R. Self-Assembled Monolayers of n-Alkanethiols Suppress Hydrogen Evolution and Increase the Efficiency of Rechargeable Iron Battery Electrodes. *J. Am. Chem. Soc.* **2013**, *135* (1), 347–353.

(12) McKerracher, R. D.; Figueredo-Rodriguez, H. A.; Alegre, C.; Aricò, A. S.; Baglio, V.; Ponce de León, C. Improving the Stability and Discharge Capacity of Nanostructured Fe2O3/C Anodes for Iron-Air Batteries and Investigation of 1-Octhanethiol as an Electrolyte Additive. *Electrochim. Acta* **2019**, *318*, 625−634.

(13) Posada, J. O. G.; Hall, P. J. Controlling Hydrogen Evolution on Iron Electrodes. *Int. J. Hydrogen Energy* **2016**, *41* (45), 20807−20817.

(14) Manohar, A. K.; Yang, C.; Malkhandi, S.; Prakash, G. K. S.; Narayanan, S. R. Enhancing the Performance of the Rechargeable Iron Electrode in Alkaline Batteries with Bismuth Oxide and Iron Sulfide Additives. *J. Electrochem. Soc.* **2013**, *160* (11), A2078−A2084.

(15) Manohar, A. K.; Malkhandi, S.; Yang, B.; Yang, C.; Surya Prakash, G. K.; Narayanan, S. R. A High-Performance Rechargeable Iron Electrode for Large-Scale Battery-Based Energy Storage. *J. Electrochem. Soc.* **2012**, *159*, A1209−A1214.

(16) Figueredo-Rodríguez, H. A.; McKerracher, R. D.; Insausti, M.; Luis, A. G.; de León, C. P.; Alegre, C.; Baglio, V.; Aricò, A. S.; Walsh, F. C. A Rechargeable, Aqueous Iron Air Battery with Nanostructured Electrodes Capable of High Energy Density Operation. *J. Electrochem. Soc.* **2017**, *164* (6), A1148−A1157.

(17) Vijayamohanan, K.; Balasubramanian, T. S.; Shukla, A. K. Rechargeable Alkaline Iron Electrodes. *J. Power Sources* **1991**, *34* (3), 269−285.

(18) Posada, J. O. G.; Hall, P. J. The Effect of Electrolyte Additives on the Performance of Iron Based Anodes for NiFe Cells. *J. Electrochem. Soc.* **2015**, *162* (10), A2036−A2043.

(19) Keersemaker, M.Critical Raw Materials. In *Suriname Revisited: Economic Potential of Its Mineral Resources*; Springer, Cham, Switzerland, 2020; pp 69−82, DOI: 10.1007/978-3-030-40268-6_9.

(20) Shangguan, E.; Fu, S.; Wu, C.; Cai, X.; Li, J.; Chang, Z.; Wang, Z.; Li, Q. Sublimed Sulfur Powders as Novel Effective Anode Additives to Enhance the High-Rate Capabilities of Iron Anodes for Advanced Iron-Based Secondary Batteries. *Electrochim. Acta* **2019**, *301*, 162−173.

(21) Deng, J.; Ye, C.; Cai, A.; Huai, L.; Zhou, S.; Dong, F.; Li, X.; Ma, X. S-Doping α-Fe2O3 Induced Efficient Electron-Hole Separation for Enhanced Persulfate Activation toward Carbamazepine Oxidation: Experimental and DFT Study. *Chem. Eng. J.* **2021**, *420* (P1), 129863.

(22) Yang, C.; Manohar, A. K.; Narayanan, S. R. A High-Performance Sintered Iron Electrode for Rechargeable Alkaline Batteries to Enable Large-Scale Energy Storage. *J. Electrochem. Soc.* **2017**, *164* (2), A418−A429.

(23) Du, J.; Bao, J.; Fu, X.; Lu, C.; Kim, S. H. Mesoporous Sulfur-Modified Iron Oxide as an Effective Fenton-like Catalyst for Degradation of Bisphenol A. *Appl. Catal. B Environ.* **2016**, *184*, 132−141.

(24) Rodríguez, H. A. F.; McKerracher, R. D.; de León, C. P.; Walsh, F. C. Improvement of Negative Electrodes for Iron-Air Batteries: Comparison of Different Iron Compounds as Active Materials. *J. Electrochem. Soc.* **2019**, *166* (2), A107−A117.

(25) Balasubramanian, T. S.; Shukla, A. K. Effect of Metal-Sulfide Additives on Charge/Discharge Reactions of the Alkaline Iron Electrode. *J. Power Sources* **1993**, *41* (1−2), 99−105.

(26) Rajan, A. S.; Ravikumar, M. K.; Priolkar, K. R.; Sampath, S.; Shukla, A. K. Carbonyl-Iron Electrodes for Rechargeable-Iron Batteries. *Electrochem. Energy Technol.* **2014**, *1*, 2−9.

(27) Gil Posada, J. O.; Hall, P. J. Post-Hoc Comparisons among Iron Electrode Formulations Based on Bismuth, Bismuth Sulphide, Iron Sulphide, and Potassium Sulphide under Strong Alkaline Conditions. *J. Power Sources* **2014**, *268*, 810−815.

(28) Siriwardane, R. V.; Poston, J. A.; Fisher, E. P.; Shen, M. S.; Miltz, A. L. Decomposition of the Sulfates of Copper, Iron (II), Iron (III), Nickel, and Zinc: XPS, SEM, DRIFTS, XRD, and TGA Study. *Appl. Surf. Sci.* **1999**, *152* (3), 219−236.

(29) Briggs, D. Handbook of X-Ray Photoelectron Spectroscopy C. D. Wanger, W. M., Riggs; L. E., Davis; J., F.; Moulder and G. E. Muilenberg Perkin-Elmer Corp., Physical Electronics Division, Eden Prairie, Minnesota, USA, 1979. 190 Pp. *Surf. Interface Anal.* **1981**, *3* (4), v−v.

(30) Brion, D. Etude Par Spectroscopie de Photoelectrons de La Degradation Superficielle de FeS2, CuFeS2, ZnS et PbS a l'air et Dans l'eau. *Appl. Surf. Sci.* **1980**, *5* (2), 133−152.

(31) Descostes, M.; Mercier, F.; Thromat, N.; Beaucaire, C.; Gautier-Soyer, M. Use of XPS in the Determination of Chemical Environment and Oxidation State of Iron and Sulfur Samples: Constitution of a Data Basis in Binding Energies for Fe and S Reference Compounds and Applications to the Evidence of Surface Species of an Oxidized Py. *Appl. Surf. Sci.* **2000**, *165* (4), 288−302.

(32) Laajalehto, K.; Kartio, I.; Suoninen, E. XPS and SR-XPS Techniques Applied to Sulphide Mineral Surfaces. *Int. J. Miner. Process.* **1997**, *51* (1−4), 163−170.

(33) Gotić, M.; Musić, S. Mössbauer, FT-IR and FE SEM Investigation of Iron Oxides Precipitated from FeSO4 Solutions. *J. Mol. Struct.* **2007**, *834−836*, 445−453.

(34) de Oñate Martínez, J.; Aguila, C. D.; Bertrán, J. F.; Ruíz, E. R.; Vergara, C. P.; Malherbe, R. R. Tribochemical Reactions of Erionite and Na-LTA Zeolites with Fe2 (SO4) 3.5 H2O: A Mössbauer Study. *Hyperfine Interact.* **1992**, *73* (3), 371−375.

(35) Rodriguez-Carvajal, J.FULLPROF: A Program for Rietveld Refinement and Pattern Matching Analysis. In *Satellite Meeting on Powder Diffraction of the XV Congress of the IUCr (Vol. 127)*; IUCr, 1990.

(36) Vandenberghe, R. E.; Barrero, C. A.; Da Costa, G. M.; Van San, E.; De Grave, E. Mössbauer Characterization of Iron Oxides and (Oxy)Hydroxides: The Present State of the Art. *Hyperfine Interact.* **2000**, *126* (1−4), 247−259.

(37) Sidhu, P. S. Transformation of Trace Element-Substituted Maghemite To Hematite. *Clays Clay Miner.* **1988**, *36* (1), 31−38.

(38) Zhou, W.; Tang, K.; Zeng, S.; Qi, Y. Room Temperature Synthesis of Rod-like FeC2O4· 2H2O and Its Transition to Maghemite, Magnetite and Hematite Nanorods through Controlled Thermal Decomposition. *Nanotechnology* **2008**, *19* (6), 065602.

(39) Lian, S.; Wang, E.; Kang, Z.; Bai, Y.; Gao, L.; Jiang, M.; Hu, C.; Xu, L. Synthesis of Magnetite Nanorods and Porous Hematite Nanorods. *Solid State Commun.* **2004**, *129* (8), 485−490.

(40) Weinrich, H.; Come, J.; Tempel, H.; Kungl, H.; Eichel, R. A.; Balke, N. Understanding the Nanoscale Redox-Behavior of Iron-Anodes for Rechargeable Iron-Air Batteries. *Nano Energy* **2017**, *41*, 706−716.

(41) Muller-Zulow, B.; Kipp, S.; Lacmann, R.; Schneeweiss, M.A. Topological Aspects of Iron Corrosion in Alkaline Solution by Means of Scanning Force Microscopy (SFM). *Surf. Sci.* **1994**, *311*, 153−158.

(42) Dražić, D. M.; Hao, C. S. The Anodic Dissolution Process on Active Iron in Alkaline Solutions. *Electrochim. Acta* **1982**, *27* (10), 1409−1415.

(43) Dıez-Pérez, I.; Gorostiza, P.; Sanz, F.; Müller, C. First Stages of Electrochemical Growth of the Passive Film on Iron. *J. Electrochem. Soc.* **2001**, *148* (8), B307.

(44) Lee, D. C.; Lei, D.; Yushin, G. Morphology and Phase Changes in Iron Anodes Affecting Their Capacity and Stability in Rechargeable Alkaline Batteries. *ACS Energy Lett.* **2018**, *3* (4), 794−801.

(45) Weinrich, H.; Gehring, M.; Tempel, H.; Kungl, H.; Eichel, R. A. Impact of the Charging Conditions on the Discharge Performance of Rechargeable Iron-Anodes for Alkaline Iron-Air Batteries. *J. Appl. Electrochem.* **2018**, *48* (4), 451−462.

(46) Kitamura, H.; Zhao, L.; Hang, B. T.; Okada, S.; Yamaki, J. Effect of Binder Materials on Cycling Performance of Fe2O3 Electrodes in Alkaline Solution. *J. Power Sources* **2012**, *208*, 391−396.

(47) Vijayamohanan, K.; Shukla, A. K.; Sathyanarayana, S. Kinetics of Electrode Reactions Occurring on Porous Iron Electrodes in Alkaline Media. *J. Electroanal. Chem.* **1990**, *295* (1−2), 59−70.

(48) Shangguan, E.; Guo, L.; Li, F.; Wang, Q.; Li, J.; Li, Q.; Chang, Z.; Yuan, X. Z. FeS Anchored Reduced Graphene Oxide Nanosheets as Advanced Anode Material with Superior High-Rate Performance for Alkaline Secondary Batteries. *J. Power Sources* **2016**, *327*, 187−195.

(49) Narayanan, S. R. R.; Prakash, G. K. K. S. S.; Manohar, A.; Yang, B.; Malkhandi, S.; Kindler, A. Materials Challenges and Technical Approaches for Realizing Inexpensive and Robust Iron-Air Batteries for Large-Scale Energy Storage. *Solid State Ionics* **2012**, *216*, 105−109.

(50) Kitamura, H.; Zhao, L.; Hang, B. T.; Okada, S.; Yamaki, J. I. Effect of Binder Materials on Cycling Performance of Fe2O3 Electrodes in Alkaline Solution. *J. Power Sources* **2012**, *208*, 391−396.

(51) Yang, J.; Chen, J.; Wang, Z.; Wang, Z.; Zhang, Q.; He, B.; Zhang, T.; Gong, W.; Chen, M.; Qi, M.; Coquet, P.; Shum, P.; Wei, L. High-Capacity Iron-Based Anodes for Aqueous Secondary Nickel-Iron Batteries: Recent Progress and Prospects. *ChemElectroChem* **2021**, *8* (2), 274−290.

(52) Manohar, A. K.; Yang, C.; Narayanan, S. R. The Role of Sulfide Additives in Achieving Long Cycle Life Rechargeable Iron Electrodes in Alkaline Batteries. *J. Electrochem. Soc.* **2015**, *162* (9), A1864−A1872.

(53) Wang, Q.; Wang, Y. Overcoming the Limiting Step of Fe2O3 Reduction via in Situ Sulfide Modification. *ACS Appl. Mater. Interfaces* **2016**, *8* (16), 10334−10342.

(54) Manohar, A. K.; Yang, C.; Narayanan, S. R. The Role of Sulfide Additives in Achieving Long Cycle Life Rechargeable Iron Electrodes in Alkaline Batteries. *J. Electrochem. Soc.* **2015**, *162* (9), A1864−A1872.